Materials & Design 213 (2022) 110369

Contents lists available at ScienceDirect

Materials & Design

journal homepage: www.elsevier.com/locate/matdes

Lightweight macroporous Co-Pt electrodeposited films with semi-hard-magnetic properties

Cristina Navarro-Senent [a], Konrad Eiler [a], Salvador Pané [b], Jordi Sort [a,c,*], Eva Pellicer [a,*]

[a] Departament de Física, Facultat de Ciències, Universitat Autònoma de Barcelona, E-08193 Bellaterra (Cerdanyola del Vallès), Barcelona, Spain
[b] Institute of Robotics and Intelligent Systems, Swiss Federal Institute of Technology ETH Zurich, Tannenstraße 3, 8092 Zurich, Switzerland
[c] Institució Catalana de Recerca i Estudis Avançats (ICREA), Pg. Lluís Companys 23, E-08010 Barcelona, Spain

HIGHLIGHTS

- Equiatomic macroporous Co-Pt films obtained by electrodeposition on titanium surfaces patterned with latex spheres of 215 nm in diameter.
- Annealing at 600 °C for 80 min results in coercivity enhancement from 148 to 1328 Oe while avoiding pore collapse.
- Increase in coercivity due to partial transformation of the initial disordered face-centered cubic phase to ordered face-centered tetragonal phase.
- Dense Co-Pt counterparts exhibit higher coercivity of 6.2 kOe upon annealing due to complete phase conversion.

GRAPHICAL ABSTRACT

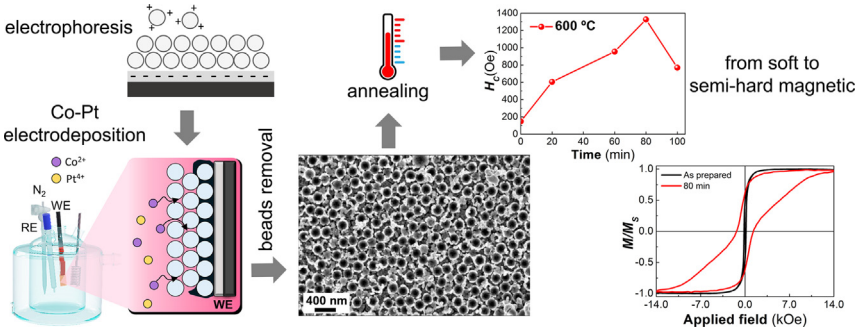

ARTICLE INFO

Article history:
Received 20 September 2021
Revised 27 December 2021
Accepted 27 December 2021
Available online 29 December 2021

Keywords:
Porous films
Co-Pt alloys
Electrodeposition
Magnetic properties

ABSTRACT

Macroporous, partially $L1_0$-ordered Co-Pt films with nearly equiatomic composition were successfully synthesized by electrodeposition from an aqueous sulfate–chloride electrolyte on colloidal crystal-templated substrates, followed by annealing in vacuum. The colloids deposited on the substrate consisted of amidine-functionalized polystyrene spheres of 215 ± 13 nm in diameter, which were self-assembled by electrophoresis. As-deposited Co-Pt films obtained after the removal of the spheres showed a highly-packed arrangement of macropores. Structurally, the films showed the A1-disordered face-centered cubic (fcc) Co-Pt solid solution, accompanied by small amounts of fcc/hexagonal close-packed (hcp)–Co. Upon annealing at 600 °C, the A1-disordered phase partly transformed into the $L1_0$-ordered (face-centered tetragonal, fct) phase. As a result, the coercivity significantly increased from 148 Oe to 1328 Oe. Importantly, the porosity of the films was preserved after annealing. Optimum annealing temperature and time were selected on the basis of a prior parametric study with electroplated dense counterparts. This work demonstrates that the combination of colloidal crystal templating and electrodeposition is a very convenient pathway towards lightweight semi-hard magnets with potential technological applications in automotive and aerospace industries, portable sensors or spectrometers, magnetic levitation systems, or magnetoelectric devices, among others.

* Corresponding authors at: Departament de Física, Facultat de Ciències, Universitat Autònoma de Barcelona, E-08193 Bellaterra (Cerdanyola del Vallès), Barcelona, Spain (J. Sort).
E-mail addresses: Jordi.Sort@uab.cat (J. Sort), Eva.Pellicer@uab.cat (E. Pellicer).

https://doi.org/10.1016/j.matdes.2021.110369
0264-1275/

1. Introduction

Hard-magnetic materials are of fundamental interest for their significant performance or key role in biomedical devices, motors, generators, recording media and microelectromechanical systems (MEMS) [1]. Currently, there is an increasing demand for small size, lightweight and low-cost hard magnets due to their potential applications in spacecraft, aircraft and portable/wireless devices, among others [2,3]. For this reason, there has been a flurry of research on the development of hard-magnetic micro/nanomaterials [4–8]. Rare-earth containing magnets (e.g. Nd-Fe-B, Sm-Co) are known as the strongest hard-magnetic materials due to their high remanent magnetization and maximum energy product $(BH)_{max}$ [1,9]. Unfortunately, rare-earth magnets are expensive and non-sustainable, suffer from high corrosion rates and their fabrication mainly relies on vacuum-based fabrication methods such as sputtering or other physical vapor deposition techniques, which are known for their high complexity and cost. In addition, they are difficult to be nanostructured or patterned into well-controlled shapes, which limits their integration in real devices [1]. Electrodeposition of rare-earth alloy magnets is a good alternative to physical deposition methods. However, their electrosynthesis from aqueous baths is not optimal because of the associated low current efficiency and incorporation of oxygen and other impurities into the films, which heavily deteriorate the hard-magnetic properties [10–12]. Alternatively, the electrodeposition of rare-earth-based magnets (in the form of films and nanowires) from deep eutectic solvents has also been demonstrated [13]. Yet, the resulting coercivity values, mainly reported for the samarium-cobalt alloy, are much lower than those achieved with sputtered films [14,15].

As an alternative to rare-earth magnets, $L1_0$-ordered alloys have emerged as candidate permanent magnets owing to their high magnetocrystalline anisotropy and large coercivity. $L1_0$-ordered alloys consist of equiatomic compositions of iron-series transitions metals (e.g. Fe or Co) and heavy transition metals (e.g. Pt or Pd), which form an asymmetric face-centered tetragonal (fct) structure (also known as $L1_0$ phase) [16,17]. Generally, the formation of $L1_0$-ordered alloys (e.g. Co-Pt, Co-Pd, Fe-Pt and Fe-Pd) requires either a high-temperature deposition or a post-deposition annealing of the as-deposited A1-disordered cubic phase to induce structural transformation into the $L1_0$-ordered phase. As opposed to rare-earth magnets, $L1_0$-ordered alloys can be prepared more easily by electrochemical deposition, both in the form of continuous thin/thick films and micro-/nanostructures, thus facilitating their implementation in micro-/nanosystems [18,19]. Although one could argue that platinum group metals (PGM) are as expensive as rare-earth metals and therefore do not represent a cheaper alternative, the supply risk of the former is lower compared to light rare-earth elements such us neodymium and samarium, according to the "Study on the EU's list of Critical Raw Materials" final report launched by the European Commission in 2020 [20]. Therefore, $L1_0$-ordered alloys certainly represent a valid alternative.

Co-Pt is among the most investigated $L1_0$-ordered systems. It exhibits a high uniaxial magnetocrystalline anisotropy (4.9 erg cm^{-3}) and $(BH)_{max}$ of 200 kJ m^{-3} [21]. $L1_0$-ordered Co-Pt alloys are usually fabricated by physical vapor deposition [22,23] or electrochemical deposition techniques [24–26], mostly in the form of dense thick and thin films owing to the high temperature treatment required for the $L1_0$-ordered phase transformation. High-temperature annealing is known to cause interdiffusion or even the collapse, for example, of arrays of substrate-supported 1D nanostructures like nanowires and nanorods [27,28].

From a manufacturing perspective, electrodeposition of $L1_0$-ordered Co-Pt alloys has garnered significant attention because it offers good shape fidelity and easy scalability at low cost [29]. The vast majority of studies have focused on the electrodeposition of thick and thin films from electrolytes containing either the dinitritodiammineplatinum ($Pt(NH_3)_2(NO_2)_2$) [24,30–34] or the hexachloroplatinate salts [35,36], the Co precursor and a few additives. Although electrodeposition has proven effective for the fabrication of low-dimensional materials [37], the preparation of miniaturized $L1_0$-ordered Co-Pt alloy in the form of nanostructured films [38] and submicron/nanostructures such as nanoparticles and pillars [39,40] has been scarcely reported. Notably, the influence of electrode surface (Ru, Cu, brass) has been investigated in a number of studies, aimed at achieving large coercivities already in the as deposited state [41].

Several approaches have been proposed for the preparation of porous metallic films via electrodeposition, using (i) soft templates such as hydrogen bubbles [42,43] or block copolymers [44,45], and (ii) hard templates like anodic alumina membranes [46,47]. Among these, colloidal crystal templating (also known as nanoscale lithography) is a cost-effective, straightforward and facile approach for the fabrication of 3D porous structures with controllable pore size. This approach relies on the self-assembly of colloid particles of varying size (typically from hundreds to tens of nanometers) onto a substrate to create a pattern of colloids, which serve as a soft or hard template [48]. Several deposition techniques can be utilized to self-assemble the colloids on a surface, such as dip-coating [49], spin coating [50] or electrophoretic deposition [51]. Essentially, the combination of two electrically driven processes, herein electrophoretic colloidal crystal templating followed by electrodeposition, represents a versatile and powerful bottom-up method to fabricate pseudo-ordered macro- or mesoporous alloy films [52–54]. From an industrial point of view, the two techniques are sufficiently mature, which makes this approach compatible with a wealth of manufacturing approaches [55,56]. Colloidal crystal templating could be also combined with physical vapor deposition techniques, but shadowing effects that create discontinuities in the film would then be encountered. Moreover, since electrodeposition works at ambient pressure, it is generally more cost effective.

The introduction of porosity into hard magnets, such as $L1_0$-ordered alloys, opens a new route to develop advanced magnetic materials which could find applications in several technological fields. Given their large $(BH)_{max}$ and porous structure, these materials have a great potential for applications which require low-density magnets such as spacecraft, automobile or microbial fuel cell technologies [57,58]. Also, the possibility to develop magnetic composites using porous hard magnets as a scaffold to be filled with other materials having different physical properties is of technological relevance. For instance, the pores could incorporate a soft-magnetic phase (yielding an exchange spring magnet material) or could be filled with an antiferromagnetic material, giving rise to a magnetic composite exhibiting exchange bias [59], a phenomenon commonly exploited in spintronic systems, magnetic random-access memories and magnetic read heads [60].

Herein, we present the fabrication of macroporous Co-Pt thin films via colloidal crystal template-assisted electrodeposition. A close-packed colloid assembly of charged amidine polystyrene (PS) spheres with a nominal diameter of 200 nm was obtained on a titanium surface by electrophoretic deposition. Subsequently, equiatomic Co-Pt alloy was grown by potentiostatic electrodeposition from a simple, additive-free aqueous electrolyte. Finally, selective etching of the spheres yielded a macroporous, nearly equiatomic Co-Pt alloy film. For the sake of comparison, fully dense films were deposited on unpatterned titanium surfaces. Both fully dense and macroporous Co-Pt films were subjected to a parametric study to determine the optimal conditions (temperature and time) to maximize the extent of conversion of the as-deposited fcc phase

into the $L1_0$-ordered (fct) phase, which was followed by both grazing incidence X-ray diffractometric (GIXRD) and vibrating sample magnetometric (VSM) studies.

2. Materials and methods

2.1. Cell and electrodes preparation

Electrodeposition was carried out in a one-compartment, thermostated three-electrode cell connected to a PGSTAT204 Autolab potentiostat/galvanostat (Metrohm-Autolab). A double-junction Ag|AgCl (E= +0.210 V/SHE) reference electrode (Metrohm AG) with 3 M KCl inner solution and 1 M Na_2SO_4 outer solution was used. A platinum spiral served as the counter electrode. All potentials quoted throughout the text are referred to Ag|AgCl (3 M KCl). Cyclic voltammetry (CV) curves were recorded on a glassy carbon electrode of 0.0314 cm^2 working area. For the preparation of dense Co-Pt thin films, flat Si/Ti (150 nm) substrates were used as working electrodes. Titanium was chosen as the metallization layer in order to provide electrical conductivity while minimizing or avoiding atomic interdiffusion in the Co-Pt thin films during post-annealing treatment. It was observed that if gold was used as the metallization layer, it diffused towards the Co-Pt alloy upon heat treatment. The working area for electrodeposition was measured to be 0.25 ± 0.01 cm^2. For the growth of macroporous Co-Pt thin films, Si/Ti (150 nm) substrates coated with amidine-functionalized PS spheres were used.

Electrophoretic deposition of the PS spheres was performed using an Agilent B2902A power supply as voltage source and a home-made 3D-printed cell consisting of poly(methyl methacrylate) (PMMA) chamber attached to a counter electrode made of platinized titanium sheet (anode). Si/Ti (150 nm) substrates (cathode) were fixed at 0.5 cm from the counter electrode (Fig. 1a). Positively charged amidine-terminated PS sub-micrometer spheres of 200 nm nominal diameter were purchased from ThermoFisher. According to the manufacturer specifications, the particles of the acquired batch had a diameter of 220 ± 15 nm, as estimated by transmission electron microscopy. The surface charge density of the beads was 13.2 mC cm^{-2}. Remarkably, positively charged PS spheres were selected in order to be able to negatively polarize the Ti conductive layer and avoid its passivation during electrophoretic deposition, which otherwise would happen under positive polarization. An aqueous solution of 0.05% w/v of PS spheres suspension was added to the custom cell. The positively charged amidine PS spheres were deposited by applying an electric field strength of + 40 V cm^{-1} during 5 min. Subsequently, the samples were dried on a hot plate at 80 °C for 10 min to evaporate the water.

2.2. Electrodeposition of Co-Pt

The electrolyte for Co-Pt deposition consisted of 0.002 M $Na_2PtCl_6{\cdot}6H_2O$ (Merck, 98% purity), 0.2 M $CoSO_4{\cdot}7H_2O$ (Merck, ≥ 95% purity) and 0.2 M Na_2SO_4 (Merck, ≥ 99% purity). The salts were dissolved in Milli-Q (MQ) water (18.2 MΩ cm). The pH was adjusted to 2.88 by adding a few drops of 1 M H_2SO_4 solution to the electrolyte. Deposition was conducted potentiostatically at − 0.55 V during 420 s on both unpatterned and patterned Si/Ti substrates, under mild agitation (ω = 100 rpm) while simultaneously bubbling N_2 into the solution to de-aerate the electrolyte (Fig. 1b(i)). The temperature was maintained at 25 °C by circulating water throughout the external jacket of the electrochemical cell by means of an F12 Julabo thermostat. After deposition, the resulting dense thin films were rinsed with MQ water and dried in air. In the case of deposition onto the electrophoretically patterned substrates, the PS spheres were selectively etched away by immersing the samples in tetrahydrofuran overnight under agitation (ω = 400 rpm) (Fig. 1b(ii)). The resulting macroporous films where thoroughly cleaned with acetone and isopropanol, rinsed with MQ water and finally dried with N_2.

2.3. Post-deposition heat treatment

Heat treatments of the as-deposited films were carried out in a home-made set-up consisting of a high-vacuum system connected to a quartz tube located inside a 653.03 MTS high-temperature fur-

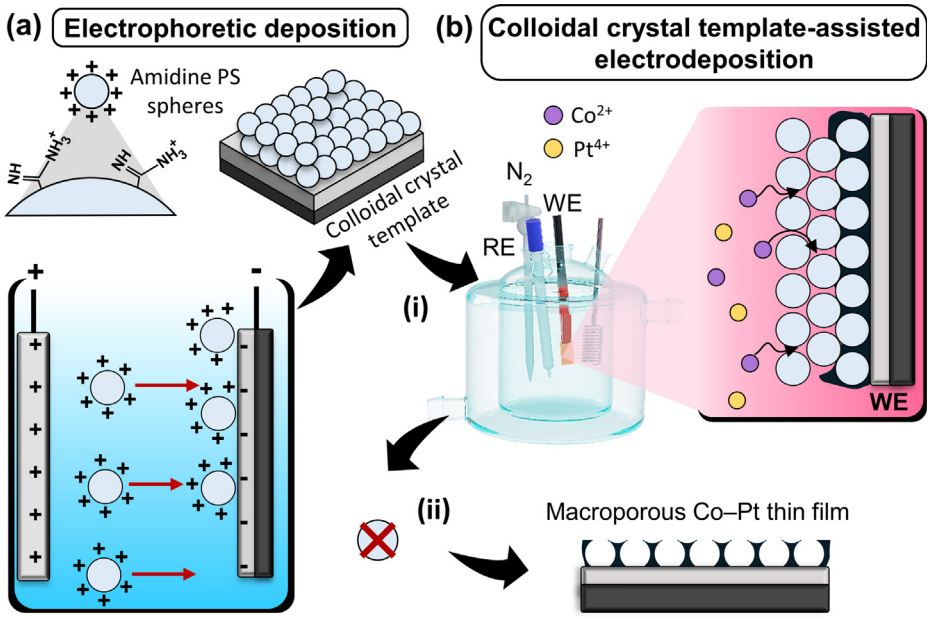

Fig. 1. (a) Schematic drawing depicting the electrophoretic deposition of PS spheres. By applying an electric field strength of 40 V cm^{-1}, positively charged amidine-terminated PS spheres move towards the cathode, resulting in the assembly of the spheres onto the Si/Ti substrate. (b) Schematic representation of colloidal crystal template-assisted electrodeposition: (i) The colloidal crystal layer is used as template for the electrodeposition of Co-Pt alloy, (ii) the PS spheres are removed, leaving the macroporous Co-Pt film behind.

nace. Annealing at different temperatures (550, 600 and 650 °C) and variable times (20, 60, 80 and 100 min) was performed under vacuum (pressure < 10^{-6} mbar). First, the furnace was heated up to the desired temperature using a ramp rate of 5 °C min^{-1}. Then, the quartz tube containing the sample under vacuum was inserted into the furnace and kept there for certain periods (20, 60, 80 and 100 min). Finally, the furnace was left to cool down to room temperature.

2.4. Characterization

A diluted suspension of PS spheres was deposited dropwise on a silicon substrate and finely metallized for imaging on a Zeiss Merlin field-emission scanning electron microscope (FE-SEM). For the sake of comparison with manufacturer specifications, 60 particles were counted to determine the mean size and standard deviation. The morphology and composition of the dense and macroporous Co-Pt films were characterized on the same microscope, which was equipped with an energy dispersive X-ray (EDX) detector. EDX analyses were carried out at 15 keV. GIXRD measurements were performed on a Bruker-AXS, model A25 D8 Discover equipped with a LinxEye XE-T detector using Cu K_α radiation and a grazing incidence angle of 1°. XRD patterns were Rietveld-fitted using the MAUD software [61] to extract the volume percentage of phases, crystallite size and microstrains. X-ray photoelectron spectroscopy (XPS) analyses were carried out on a PHI 5500 Multitechnique System spectrometer from Physical Electronics with a monochromatic X-ray source Al Kα line of 1486.6 eV energy and 350 W power, placed perpendicular to the analyzer axis and calibrated by the $3d_{5/2}$ line of Ag with a full width at half maximum (FWHM) of 0.8 eV. The analyzed area was a circle of about 0.8 mm in diameter. Magnetic measurements were carried out using a VSM from Micro sense (LOT–Quantum Design). Hysteresis loops were recorded at room temperature along the in-plane direction, with a maximum applied magnetic field of 20 kOe. Magnetization versus temperature curves were recorded under an applied magnetic field of 10 kOe from 300 K to 800 K under argon atmosphere to prevent from sample oxidation. Samples were attached to the quartz sample holder using an alumina-based bonding ceramic cement (Resbond 901 adhesive from Cotronics Corp.) that withstands 1650 °C. The corrosion behavior of the films was studied by potentiodynamic polarization (PDP) at room temperature in de-aerated 3.5 wt% NaCl solution. The films were first immersed in the NaCl solution for 30 min to determine the open circuit potential (OCP). Immediately afterwards, the potential was swept from –300 mV below the OCP towards 1.5 V beyond the OCP at 0.5 mV s^{-1} under stagnant conditions.

3. Results and discussion

The bath utilized for the deposition of Co-Pt alloy was adapted from a formulation previously devised for the deposition of Fe-Pt magnets [18]. It is an additive-free electrolyte, which simply contains sodium hexachloroplatinate and cobalt sulfate salts as electroactive species and sodium sulfate to increase bath conductivity. This bath formulation had not been used before for the synthesis of $L1_0$-ordered Co-Pt alloys. The use of complexing agents and other additives was avoided on purpose to avoid the inclusion of impurities, which could deteriorate the magnetic properties. Impurities in electrodeposited magnets form non-magnetic species with iron group metals, hence diluting magnetism within the films [62]. Fig. 2a shows the CV curves recorded from an electrolyte with the same concentrations of salts as those reported in [18] with the replacement of $FeSO_4$ by $CoSO_4$ (red dashed curve), and an electrolyte with doubled concentrations of

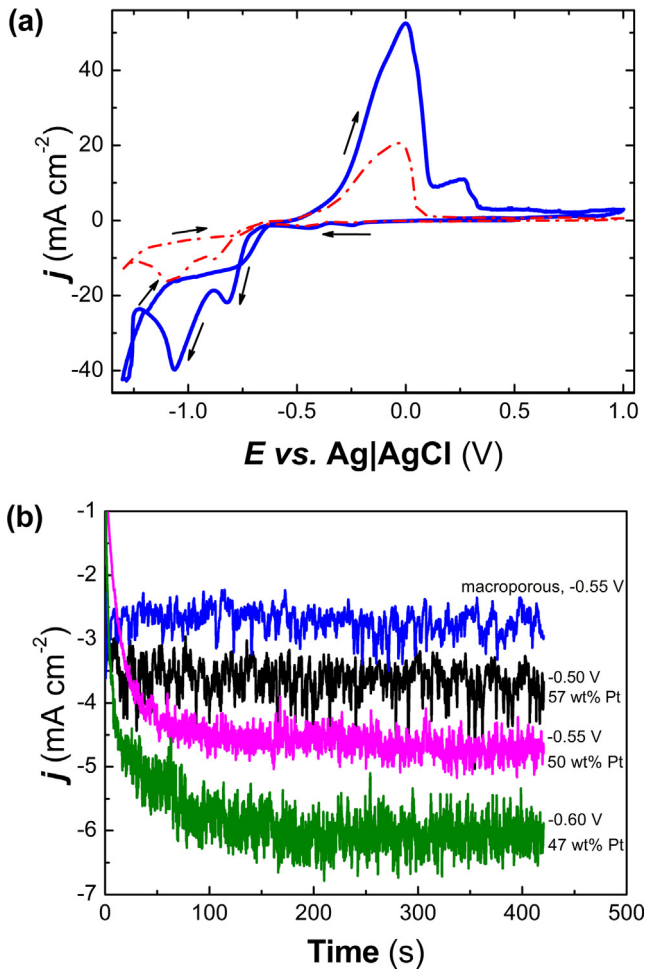

Fig. 2. (a) CV curves recorded under stationary conditions at 50 mV s^{-1} on vitreous carbon electrode from the optimized sulfate–chloride electrolyte (with 0.002 M $Na_2PtCl_6{\cdot}6H_2O$, 0.2 M $CoSO_4{\cdot}$ $7H_2O$ and 0.2 M $NaSO_4$, pH = 2.88; blue continuous line) and the electrolyte with halved concentrations of the salts (0.001 M $Na_2PtCl_6{\cdot}6H_2O$, 0.1 M $CoSO_4{\cdot}7H_2O$ and 0.1 M $NaSO_4$, pH = 2.88; red dashed line). (b) *j*-t curves recorded from the optimized electrolyte on flat Si/Ti substrates (black, magenta and green curves) under stirring conditions, at the indicated applied potentials. The corresponding Pt content (determined by EDX) in the resulting films is also given. The blue curve corresponds to the deposition on the patterned Si/Ti substrate at −0.55 V, for which the current was normalized to the geometric area of the substrate. (For interpretation of the references to colour in this figure legend, the reader is referred to the web version of this article.)

these salts (blue continuous line). Both CVs were recorded on a glassy carbon electrode under stagnant conditions and showed a similar profile. In the negative sweep, the different reduction peaks can be attributed to the discharge of Pt(IV) ions, followed by Co(II) co-deposition and hydrogen co-evolution [63]. In the anodic scan, a main oxidation peak centered at –0.015 V and a much weaker peak at more positive potentials (for the blue curve) were recorded. According to the CV fingerprint, cathodic potentials close to the onset of Co and Pt co-deposition (roughly around –0.5 V) should be screened for subsequent potentiostatic deposition of nearly equiatomic alloy compositions on Si/Ti substrates (i.e., to avoid the growth of Co-rich deposits). Deposits grew on the flat Si/Ti substrates at potentials of –0.5 V and more negative when deposition from the diluted electrolyte was attempted, but the deposition rate was very low. For this reason, the bath from doubled concentration of the salts was selected for subsequent experiments, since it yielded deposits at a higher deposition rate. Following a parametric study of the Co-Pt composition dependence on the deposition potential (Fig. 2b), a constant potential value of −0.55 V was cho-

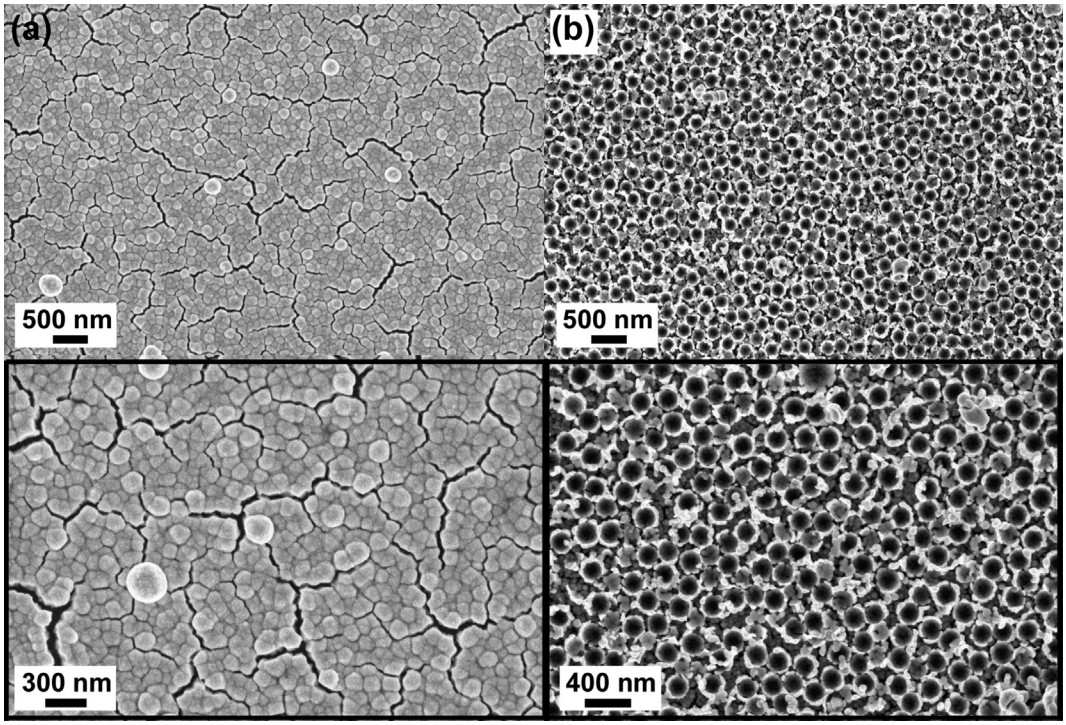

Fig. 3. Representative low and high magnification FE-SEM images of equiatomic, as-deposited (a) dense and (b) macroporous Co-Pt films deposited at −0.55 V.

sen for preparing Co-Pt deposits with equiatomic composition on unpatterned Si/Ti substrates. Deposition was conducted potentiostatically since (i) the real working area of the colloidal crystal templated substrates used for the deposition of the macroporous Co-Pt counterparts could not be precisely determined, (ii) the active surface area changes as the process proceeds, and (iii) such processes are usually driven at a relatively low rate as compared to the deposition on flat substrates because of the sluggish transport conditions. The blue curve in Fig. 2b corresponds to the *j*-t curve recorded during Co-Pt deposition on the patterned Si/Ti substrates. Note that the current was normalized by the geometric area of the substrate. If the real working area could be determined, more negative current densities would have been registered.

Fig. 3 shows representative FE-SEM images of the as-deposited, equiatomic, macroporous Co-Pt films and their dense counterparts. Dense films exhibit fine submicrometer grains with round-shaped morphology and small cracks over the entire surface (Fig. 3a). Cracks would appear due to sample drying and incipient hydrogen co-evolution.

Fig. 3b shows the FE-SEM images of the macroporous Co-Pt films after PS spheres removal. The films displayed an architecture consisting of nearly a monolayer of hemispherical randomly arranged pores. Interestingly, these were virtually crack-free, as opposed to the dense counterparts. The pore size (∼200 nm) matched the diameter of the PS spheres. For comparison purposes, Fig. 4 shows a FE-SEM image of PS spheres deposited on a silicon substrate, whose diameter was estimated as 215 ± 13 nm, hence close to the manufacturer value (220 ± 15 nm). Cross-sectional measurements of the Co-Pt coatings revealed a thickness of 201 ± 7 nm for dense films and 116 ± 4 nm for macroporous thin films. Elemental compositional analysis disregarding oxygen revealed a composition of 49 ± 4 at.% Co and 51 ± 4 at.% Pt for the fully dense films, whereas macroporous films showed a composition of 52 ± 5 at.% Co and 48 ± 5 at.% Pt. Moreover, a relatively low concentration of oxygen was found in both cases, namely 9 at.% for the dense films and 15 at.% for the macroporous films. The oxygen content is lower than that found in nearly equiatomic, dense, Fe-Pt layers electrodeposited from acidic aqueous solutions, which is around 25–30 at.% [64]. There is probably not a sole reason to explain why the here-deposited Co-Pt films show limited oxygen incorporation. First of all, iron electrochemistry is particularly tricky and the inclusion of moderately large amounts of oxygen in iron and iron alloys electrodeposited from acidic or neutral electrolytes is quite common [65,66]. Secondly, unless Fe(II) is complexed via the addition of, e.g. ascorbic acid, Fe(II) oxidation to Fe(III) takes place in the electrolyte, which eventually leads to the precipitation of ferric hydroxides [67].

The increase in both the Co and the oxygen contents in the macroporous films can be attributed to regions of increased current density at the edges of the template. In addition, the macroporous films exhibit a larger surface area. It is highly likely that the

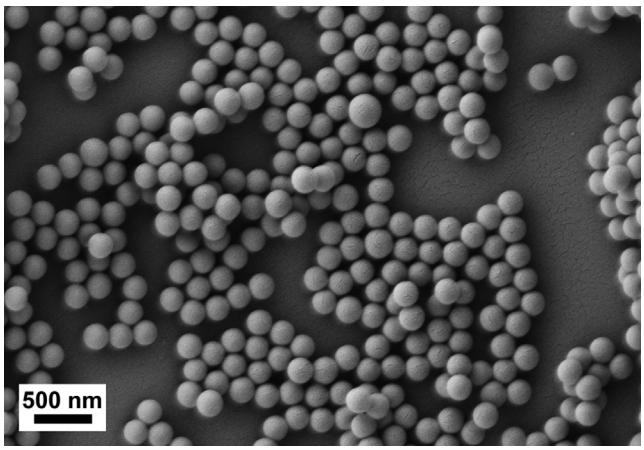

Fig. 4. FE-SEM image of the PS spheres utilized to produce macroporous Co-Pt coatings. A diluted aqueous suspension of the spheres was prepared and deposited dropwise on a silicon substrate.

small Co grains in these films tend to passivate and form an oxide layer when they are exposed to air, similar to what was observed in a previous study on the magnetic properties of macroporous Co films [68].

GIXRD analyses were performed to determine the crystallographic phases of dense and macroporous Co-Pt films both before and after annealing (Fig. 5a and b respectively). Note that GIXRD was used instead of standard Bragg-Brentano geometry because of low deposit thickness (≤200 nm), i.e., to avoid or minimize the otherwise intense signal coming from the substrate. For the sake of clarity, only the GIXRD patterns corresponding to samples annealed under optimal conditions, i.e. 600 °C for 100 min for the dense films, and 600 °C for 80 min for the macroporous Co-Pt counterparts, are shown. These are optimal annealing conditions as it

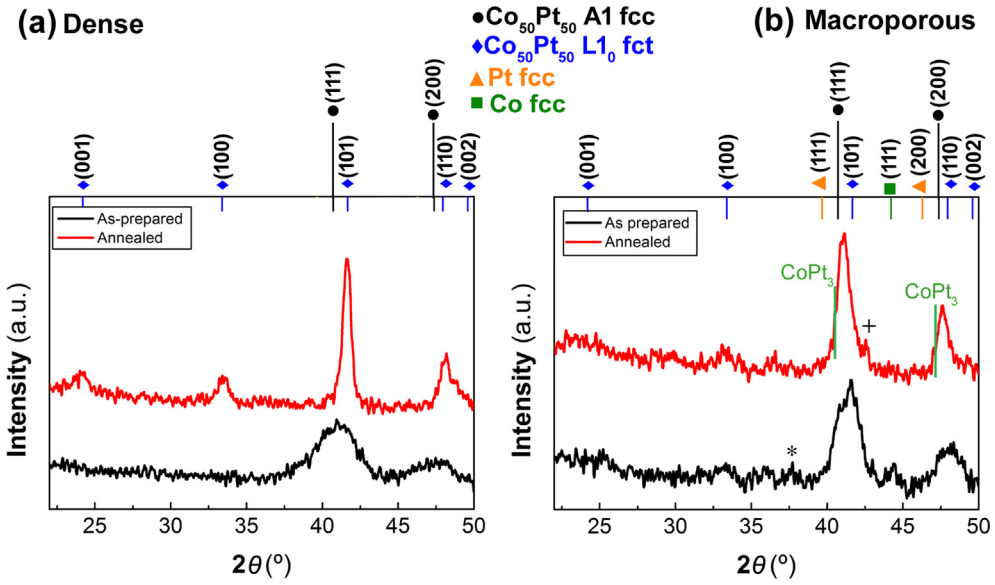

Fig. 5. XRD patterns of (a) the equiatomic dense Co-Pt films in the as-prepared state (black curve) and after being annealed at 600 °C for 100 min (red curve), and (b) the macroporous Co-Pt films in the as-prepared state (black curve) and after being annealed at 600 °C for 80 min (red curve). The peaks denoted with (+) and (*) belong to fcc-CoO and cobalt oxyhydroxides/oxides, respectively. (For interpretation of the references to colour in this figure legend, the reader is referred to the web version of this article.)

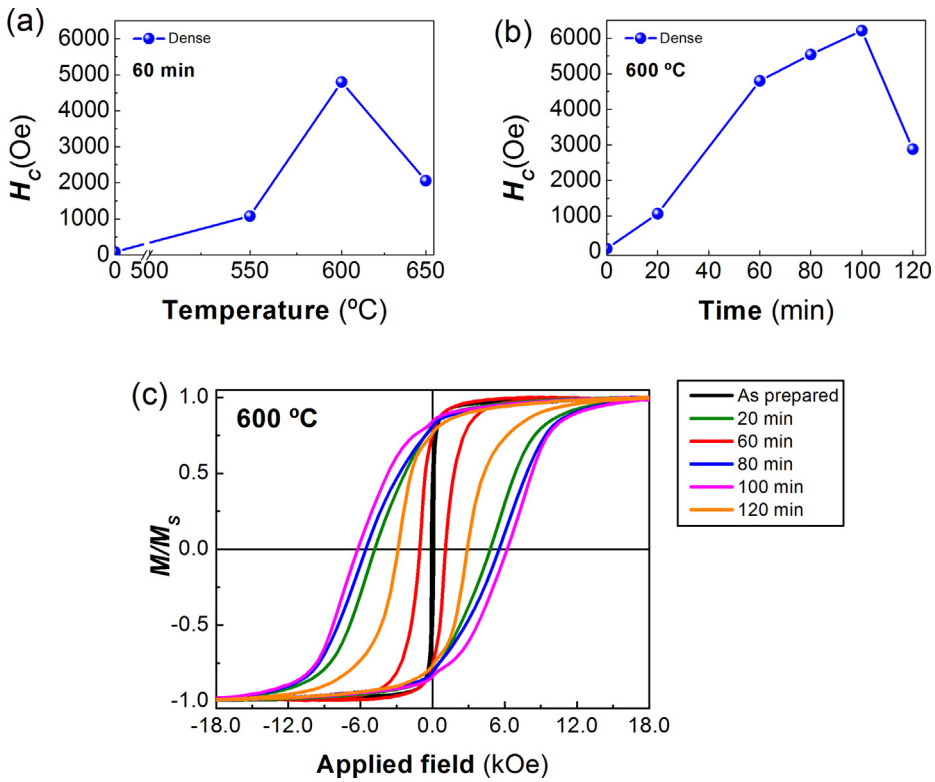

Fig. 6. (a) Dependence of H_C on temperature for a fixed annealing time of 60 min for the equiatomic dense Co-Pt films. (b) Dependence of H_C on annealing time for a fixed temperature of 600 °C. (c) In-plane hysteresis loops of the as-prepared dense Co-Pt films (black curve) and annealed at 600 °C for 20, 60, 80, 100 and 120 min.

Table 1
Summary of morphological, structural (main phases) and magnetic properties of as prepared and annealed dense and macroporous Co–Pt films. < *D* > stands for crystallite size, and vol.% for volume percentage of phase.

Sample	morphology	A1 Co–Pt			$L1_0$ Co–Pt			fcc Co			M_R/M_S	H_C (Oe)
		<*D*> (nm)	vol.%	microstrains	<*D*> (nm)	vol.%	microstrains	<*D*> (nm)	vol.%	microstrains		
As-prepared dense	dense, nodular	5	100	$8.5{\cdot}10^{-3}$	–	–	–	–	–	–	0.47	85
Annealed dense (600 °C, 100 min)	grains, cracks	–	–	–	16	100	$2.1{\cdot}10^{-3}$	–	–	–	0.84	6212
As-prepared porous	rounded pores,	8	92	$5.6{\cdot}10^{-3}$	–	–	–	16	8	$2.5{\cdot}10^{-4}$	0.47	148
Annealed porous (600 °C, 80 min)	crack-free	10	40	$4.5{\cdot}10^{-4}$	9	60	$1.6{\cdot}10^{-4}$	–	–	–	0.62	1328

will be demonstrated later in the magnetic characterization part (Figs. 6 and 9, respectively).

In the GIXRD patterns of the as-prepared dense Co-Pt films, two wide main peaks, located at 41.0° and 47.4°, that matched the (111) and (200) peaks of the fcc phase of equiatomic Co-Pt (i.e., the so-called A1-disordered phase), were observed [38]. Furthermore, the crystallite size obtained from Rietveld fitting (see Figure S1 from S.I.) was about 5 nm (Table 1). After annealing at 600 °C for 100 min, the corresponding GIXRD patterns showed narrower peaks at 24.2°, 33.4°, 41.6° and 48.2°, which are assigned to the fct $L1_0$-ordered phase. EDX analyses did not show signs of Ti seed-layer interdiffusion, in contrast to other studies in which 14 at.% of Au was detected in Co-Pt films on annealing Co-Pt/Au/Si samples annealed at 500 °C [69]. The crystallite size of the fct phase was 16 nm (Table 1). These results prove that the chosen annealing conditions efficiently promote the rearrangement of Co and Pt atoms from the A1-disordered phase into the chemically ordered $L1_0$ structure. Hosoiri et al. achieved conversion of the chemically disordered fcc phase into the fct $L1_0$-ordered in 35 μm-thick electroplated Co-Pt films with 51.1 at.% Pt at 450 °C for 60 min [35]. In turn, Oniku et al. applied higher annealing temperatures (675–700 °C) for 30 min in H_2/N_2 atmosphere [24,30] and these were optimum conditions for equiatomic Co-Pt films up to 6 μm in thickness to fully convert to $L1_0$ phase. In our work, maximum conversion of thinner (0.2 μm) dense films was achieved at an intermediate temperature (600 °C) held during a longer time period (100 min). The diffractograms of the as-deposited macroporous Co-Pt films show two main peaks located at 41.6° and 48.0°, which are compatible with the existence of an A1-disordered solid solution slightly richer in Co than the equiatomic composition [35]. Additionally, the pattern shows a small peak at 44.4° matching the position of fcc/hcp-Co and a peak at 37.5° (marked with an asterisk) that can be attributed to Co oxyhydroxides/oxides. Considering that the chemical composition of the macroporous films was 52 ± 5 at.% Co and 48 ± 5 at.% Pt, a solid solution richer in Pt should also be present. According to PDF# 004–0802, pure fcc-Pt has (111) and (200) reflections at 39.8° and 46.2°, respectively. With a small amount of Co dissolved in the fcc-Pt lattice, the corresponding reflections would shift towards higher 2θ angles, hence partly overlapping with the reflections of the A1-disordered solid solution above mentioned. The films were also nanocrystalline, with a crystallite size of 8 nm for the main fcc-Co-Pt phase and 16 nm for the minor pure Co phase, as obtained from Rietveld fitting of the XRD pattern (Table 1 and figure S1). The occurrence of various phases in the films can be explained by the absence of a complexing agent in the electrolyte and the more sluggish mass-transfer conditions compared to the unpatterned substrates.

Upon annealing, the corresponding XRD patterns showed peaks located at 23.7°, 33.0°, 41.1° and 47.6° which matched the fct $L1_0$-ordered phase. These peaks, though, are shifted towards smaller angles (by ∼ 0.5°) indicating enrichment in Pt. A small peak is observed at 42.6° (denoted with a "+" symbol in the diffractogram), which matches the position of fcc-CoO phase. Compared to the fully dense counterpart, Rietveld fitting of the diffractogram (figure S1) revealed that a fraction of untransformed A1 phase (40 vol.%) remained in the coating (Table 1). In addition, the cubic intermetallic $CoPt_3$ phase (PDF# 029–0499) could also be present, having its main peaks at 40.5° and 47.1° angular positions, as indicated in Fig. 5(b). This phase is typically formed in non-equiatomic Co-Pt alloys with deviations of the order of 5 at.% [70]. The annealed macroporous samples remained nanocrystalline, with crystallite sizes of 10 nm and 9 nm for the fcc and fct phases, respectively (Table 1).

The experimental I(111)/I(200) ratio for the as-prepared dense film (2.7) is close to that of the theoretical fcc-$Co_{50}Pt_{50}$ phase with randomly oriented grains (2.5). The same is true for the as-prepared macroporous film (I(111)/I(200) = 2.6). Therefore, the fcc phase is not or little textured. Meanwhile, although the (111) reflection is also theoretically the most intense reflection of the fct phase (PDF no. 00–043-1358), the annealed macroporous film is slightly textured along the (200) plane. The theoretical I(111)/I(200) ratio of the isotropic $L1_0$ phase is 2.7 and the corresponding ratios for the dense and macroporous films are 2.7 and 2.0, respectively.

As-deposited, dense Co-Pt thin films were magnetically soft with a coercivity (H_C) of 85 ± 5 Oe. A first parametric study to determine the optimal annealing conditions was performed on the fully dense films (Fig. 6). First, the temperature was optimized for a fixed annealing time of 60 min, as seen in Fig. 6a. As the annealing temperature was made higher, H_C values increased, suggesting that the disordered phase gradually converted into the $L1_0$-ordered phase. The H_C reached the highest value of 4.8 kOe when the dense films were annealed at 600 °C but it dropped to 2.0 kOe when the annealing temperature was set at 650 °C. From the observed results, it was concluded that 600 °C was the optimum temperature for the structural conversion from the as deposited fcc to the fct phase. Later, annealing time was optimized while keeping the optimum temperature of 600 °C fixed (Fig. 6b and c). On increasing the annealing time from 20 to 100 min, H_C increased monotonically from 1.06 kOe after 20 min to 6.2 kOe after 100 min, and then dropped to 2.8 kOe when the film was annealed for 120 min, as shown in Fig. 6b. Similar observations were made by other authors which attributed the decline in coercivity to grain growth [70,71]. Our maximum coercivity values are in agreement with other studies devoted to the electrodeposition of Co-Pt and Fe-Pt films followed by annealing in vacuum to induce the fcc to fct transformation. For example, Yanai et al. achieved H_C values of 8.5 kOe on average with annealing equiatomic Fe-Pt thick films [72]. Yet, higher coercivities have been reported for nanocrystalline electrodeposited Fe-Pt films upon annealing under a reducing atmosphere, on the order of 11–14 kOe [73,74].

In contrast to as-deposited dense films, annealed counterparts showed squarer hysteresis loops with a squareness ratio closer to 1, which is a characteristic of hard-magnetic materials (Fig. 6c). Moreover, all the annealed films showed a nearly single-phase

magnetic character. From these results, it was concluded that 600 °C and 100 min were the optimal annealing conditions to achieve maximum conversion of the as-obtained phase into the $L1_0$-ordered one for the dense Co-Pt thin films. Interestingly, no $L1_0$ ordering was observed in electrodeposited Co-Pt films annealed up to 500 °C by Rozman et al. [75], who observed that the formation of the fct phase started upon annealing at 600 °C for 60 min and maximum conversion was achieved at 700 °C (1.17 T), hence under conditions similar to our work.

Fig. 7 shows the FE-SEM images of the dense Co-Pt films before and after annealing at 600 °C for 100 min. Interestingly, no pronounced changes in morphology were observed after heat treatment. Yet, grains became a bit less rounded and the width of the cracks increased (Fig. 7b), which could be attributed to recrystallization induced by the annealing process.

Concerning macroporous Co-Pt thin films, they are magnetically soft in the as-prepared state, with a slightly higher H_C (148 ± 9 Oe) compared to the fully dense films, probably due to the hindrance imposed by the pore walls on the propagation of magnetic domain walls. Since the annealing temperature had been previously optimized for the dense films, we decided to subject the macroporous thin films to the same temperature for varying annealing times.

Fig. 8 shows the corresponding in-plane hysteresis loops and the FE-SEM images of the resulting annealed films. As the annealing time was increased, wider loops were obtained, analogous to what was observed for the dense films. In addition, the macroporous Co-Pt film annealed at 600 °C shows a two-phase magnetic behavior (Fig. 8c), which is particularly obvious for an annealing time of 80 min. This could be anticipated from the GIXRD analysis, which revealed the co-existence of several phases (Pt-rich Co-Pt $L1_0$-ordered and soft magnetic $CoPt_3$ besides the nearly equiatomic fcc phase). Ying et al. also observed a shoulder in the hysteresis loops upon annealing electrodeposited Fe-Pt films at 800 °C, which the authors attributed to the coexistence of the soft-magnetic fcc phase and the hard-magnetic $L1_0$ phase [74]. Regarding the morphology, no significant variations were observed as the annealing time increased and, most importantly, porosity was preserved in all the samples after the heat treatment. This is opposite to what it had been observed in mesoporous Co-Pt films (20-nm pore size) prepared by micelle-assisted electrodeposition [76], where annealing at 600 °C for 60 min resulted in a collapse of the mesopores, giving rise to non-porous deposits. Thus, the selection of the proper pore size is important in this kind of material to avoid pores collapsing during heat treatments, which are aimed for the semi hard-magnetic phase evolution.

Fig. 9a shows the evolution of H_C as a function of the annealing time (keeping $T_{annealing}$ = 600 °C) for the macroporous Co-Pt thin films. As the annealing time increased, H_C augmented progressively and reached a maximum of 1328 Oe after 80 min. Afterwards, H_C dropped to 770 Oe when the annealing time was extended to 100 min. The increase in H_C with the annealing time was primarily explained by the extent of the conversion from fcc into fct phase. Rietveld fitting of the XRD pattern of the film heat-treated for 20 min showed the presence of 43 vol.% of $L1_0$ phase (see Figure S2 in the S.I. file), whereas this percentage increased to 60 vol.% for the macroporous coating treated for 80 min (Table 1). In any case, the increase in H_C was much less pronounced than for the fully dense counterparts. First, the as-deposited macroporous films were structurally different from the dense counterparts and consisted of a mixture of phases, as evidenced by GIXRD. Secondly, the transformation resulted in a mixture of nearly equiatomic fcc Co-Pt phase, $L1_0$-ordered Pt-rich Co-Pt alloy and CoO phases. Meanwhile, the percentage of $L1_0$-ordered phase for the macroporous coating was 60 vol.%, whereas for the dense film full conversion was achieved (Table 1). As can be seen in Fig. 9b, the macroporosity was preserved across the film surface after the heat treatment. Roughly half empty spheres are seen from the cross-section (top panel in Fig. 9c), which corresponds to half the diameter of the spheres (215 nm) and approximately matches the measured film thickness (116 nm). Yet, less rounded macropores were found after annealing which could be attributed to the deformation of the pore wall (cf. Fig. 3a and 8d). The same can be said in terms

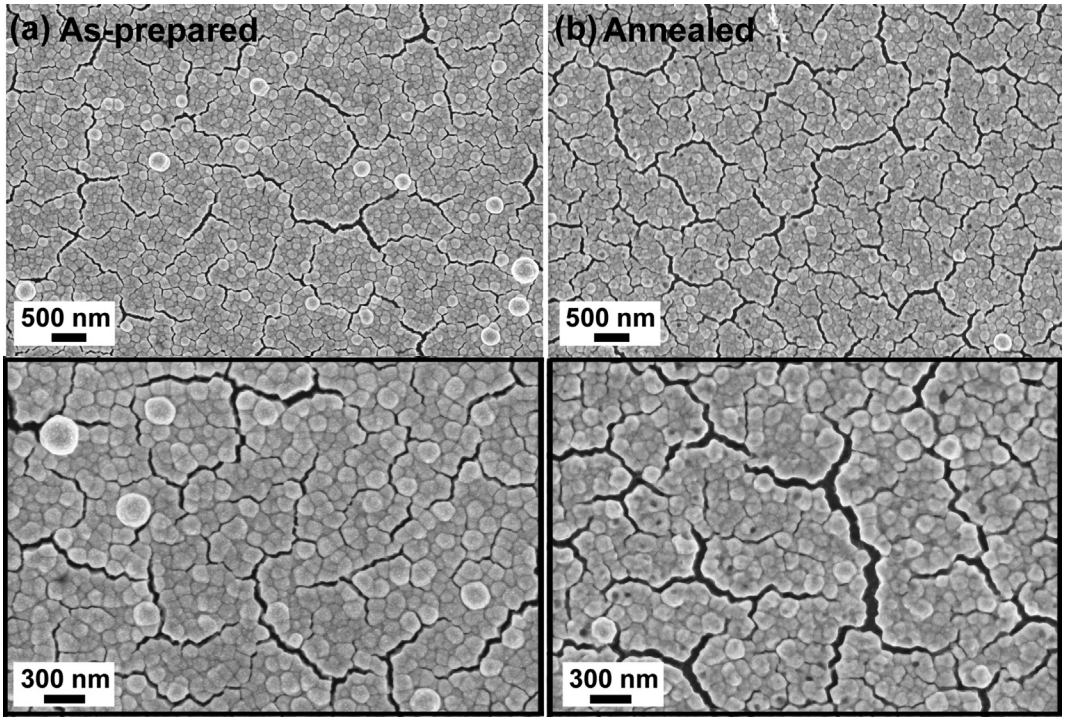

Fig. 7. Low and high magnification FE-SEM images of the equiatomic dense Co-Pt thin films (a) before and (b) after annealing at 600 °C for 100 min.

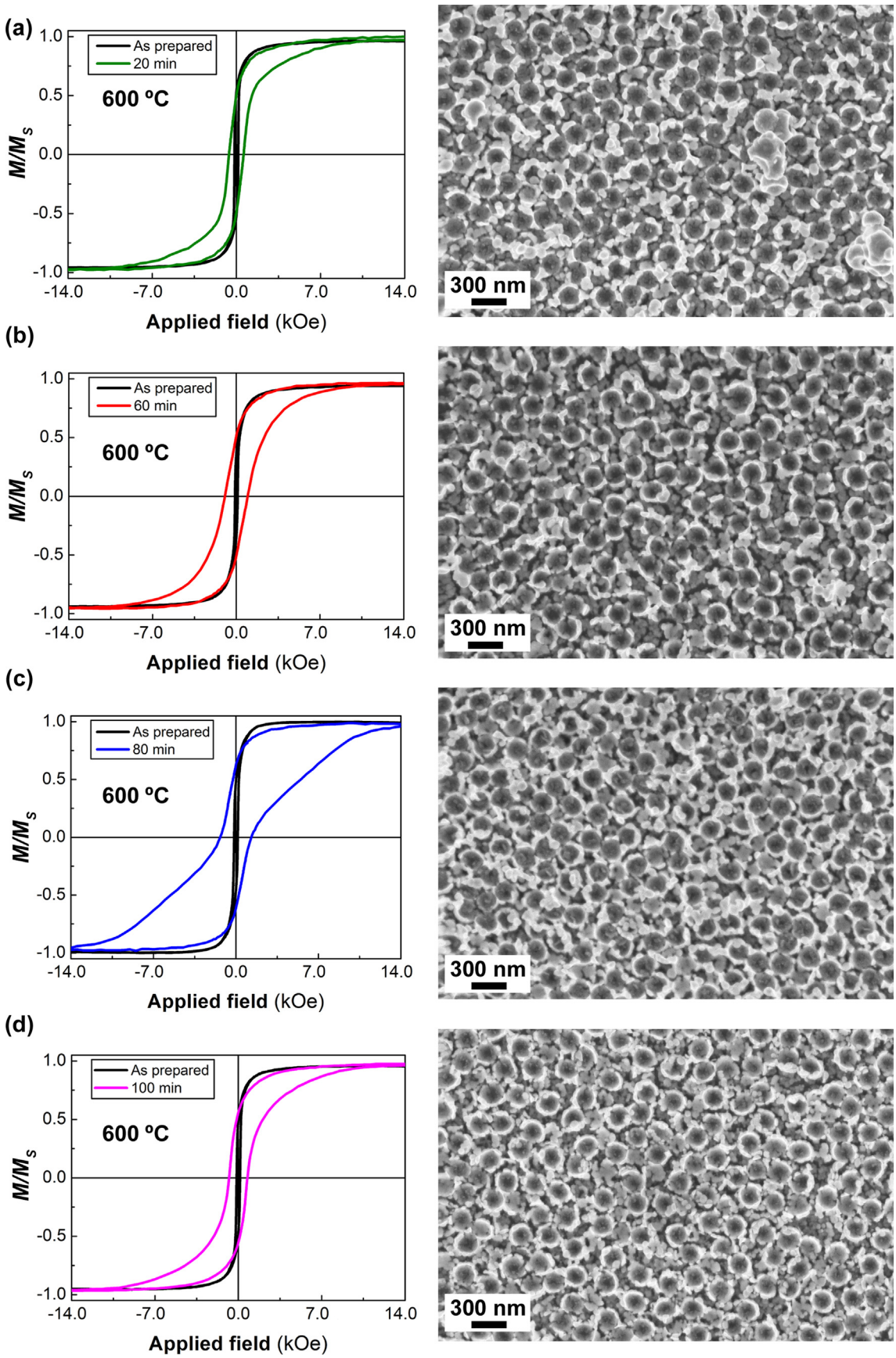

Fig. 8. In-plane hysteresis loops of the as-prepared macroporous Co-Pt films (black curve) and after annealing at 600 °C for (a) 20 (b) 60 (c) 80 and (d) 100 min and their corresponding FE-SEM images.

of film thickness for the annealed dense counterpart (bottom panel in Fig. 9c), which is added here for the sake of comparison. Finally, no pronounced differences were observed between hysteresis loops measured along different angles (from in-plane to perpendicular-to-plane directions) (Fig. 10). Only a slight reduction in the squareness ratio (M_R/M_S) and a slightly more tilted loop shape were observed for the dense films (from M_R/M_S = 0.84 along the film plane to M_R/M_S = 0.73 along the perpendicular-to-plane direction) (Fig. 10a). The porous films exhibit a very isotropic magnetic response (Fig. 10b). This can be due to the polycrystalline character of the films and the eventual role of porosity in disrupting the in-plane geometry of the films. The magnetization versus temperature curves of the annealed films show a progressive decrease of magnetization till 800 K, at which the magnetization

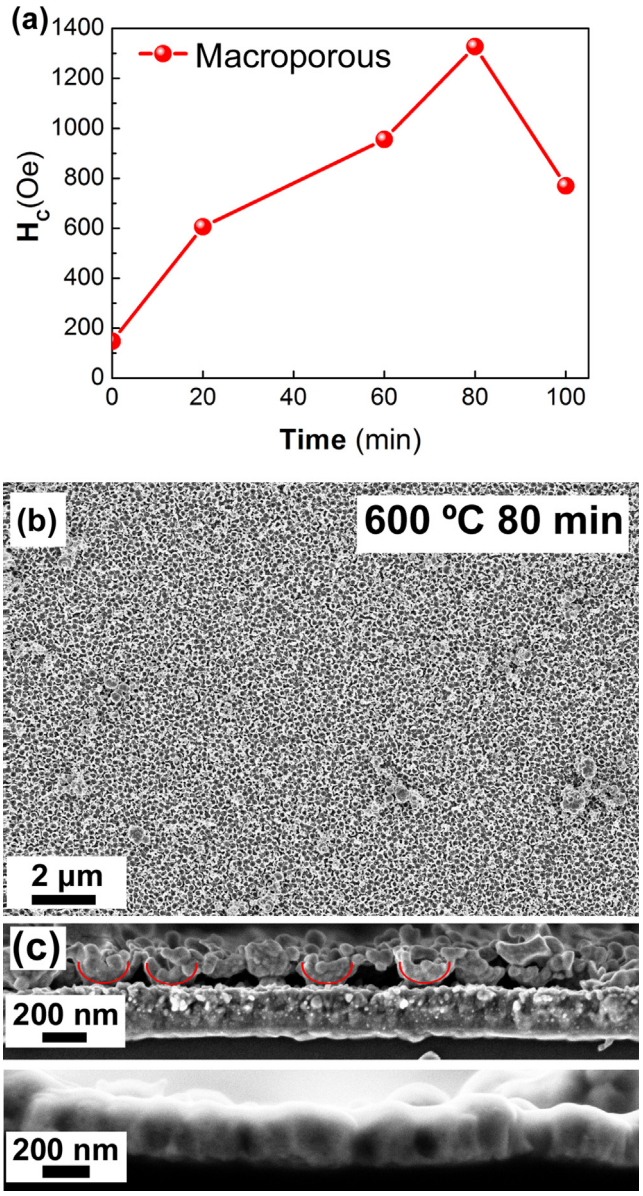

Fig. 9. (a) Dependence of H_C on annealing time for a fixed temperature of 600 °C for the macroporous Co-Pt thin films, (b) Low magnification top-view, and (c) cross-section FE-SEM images of (top panel) annealed macroporous nearly equiatomic Co-Pt film at 600 °C for 80 min and (bottom panel) annealed dense counterpart at 600 °C for 100 min. The red semicircles in panel (c) show the profile of half empty spheres, which is the cross-sectional pattern left in the material following removal of the 215 nm-sized spheres. (For interpretation of the references to colour in this figure legend, the reader is referred to the web version of this article.)

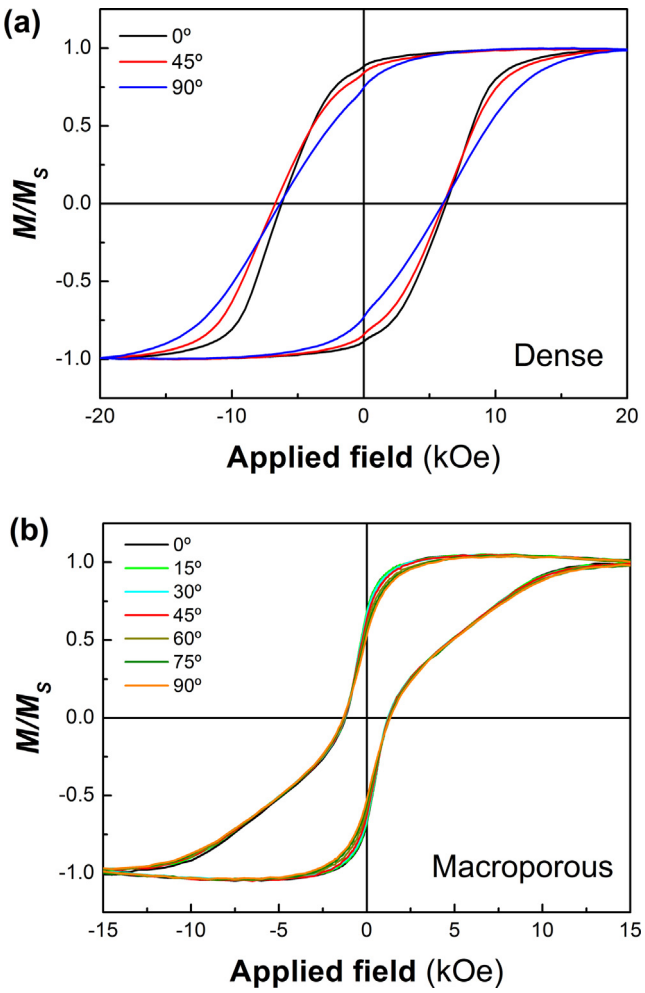

Fig. 10. Angular dependence of the normalized hysteresis loops for annealed (a) dense and (b) macroporous Co-Pt films.

is almost zero (Figure S3 in the S.I. file). This agrees with the reported Curie temperature (T_C) for $L1_0$ and fcc Co-Pt alloys (T_C in the range 750 – 900 K) [77,78].

Fig. 11 shows SEM-EDX mappings of the annealed dense and porous samples. Specimens were tilted inside the SEM chamber to capture signal from both on top and cross-sections. The distribution of Co and Pt elements was homogeneous in both samples and the O signal was a bit higher for the macroporous film, in agreement with the findings from the as-deposited state. Note that oxygen signal has two sources (the Co-Pt layer itself and the substrate beneath, as revealed after mapping a naked substrate). The Ti and Si signals are particularly elevated in the region covered by the ferromagnetic macroporous film, which is due to the fact that mapping was done on one edge of the specimen, and the porous character of the Co-Pt film.

Considering the presence of oxygen in the coatings, XPS analyses were carried out to probe the oxidation state of Co in the films. The Co 2p core-level binding energies of 778 and 780 eV correspond to metallic and oxidized Co, respectively (Fig. 12). Note that all common cobalt oxides and hydroxides exhibit very similar binding energies around 780 eV, so that an exact determination of the oxidized species is not possible and may even include Co (III) (such as in CoOOH) [79]. Notably, metallic Co is the main signal and the presence of cobalt oxides can be largely ascribed to surface passivation. For completeness, the O1s signal is given in Figure S4 of the S.I. file. After sputtering the films for 1 min with

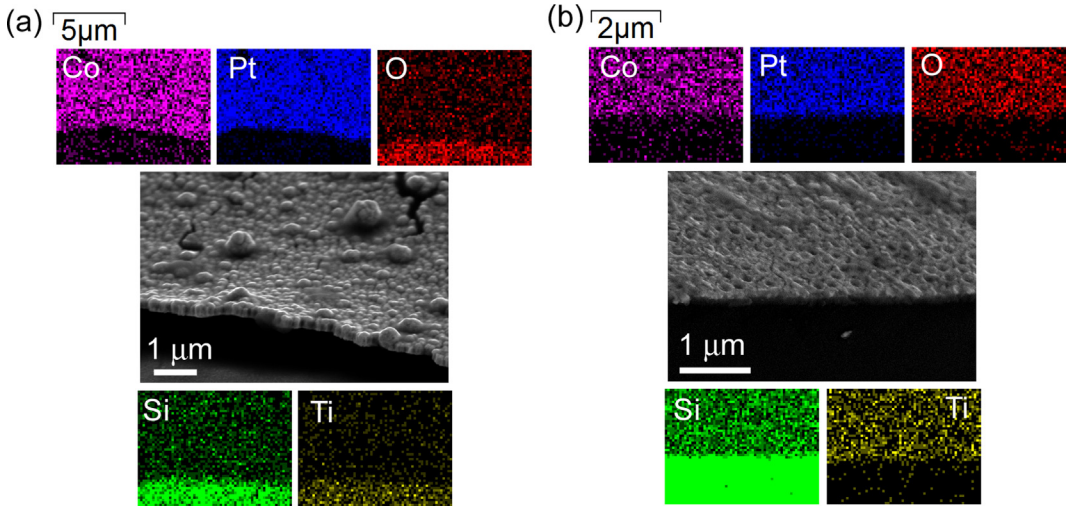

Fig. 11. SEM image and corresponding EDX mappings (Co, Pt, O, Si, and Ti) taken on the annealed (a) dense and (b) macroporous films.

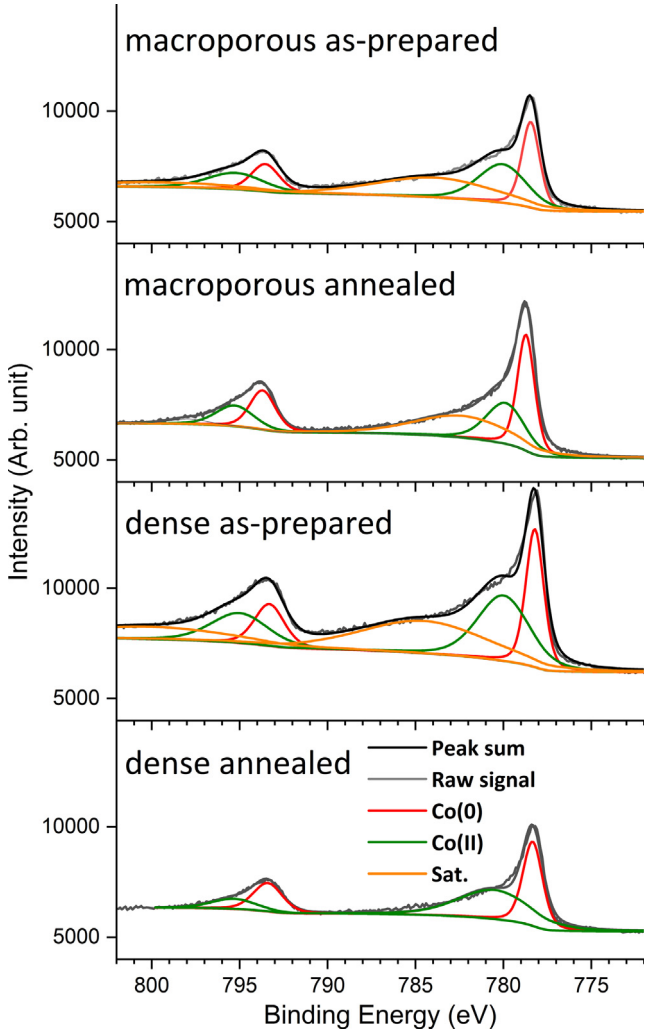

Fig. 12. Co 2p core-level XPS spectra for as prepared and annealed macroporous and dense films. Annealing was conducted at the optimal conditions (600 °C, 100 min for dense film and 600 °C, 80 min for macroporous film).

Ar^+ to remove the outmost passivation layer, the oxygen signal declined .

For the sake of clarity, the morphological, structural and magnetic properties of as deposited and annealed dense and macroporous films at the optimal temperatures and times are gathered in Table 1. Although annealing does not endow the macroporous Co-Pt films with hard-magnetic properties, the films are crack-free. The H_C values seem to largely correlate with the extent of fcc to fct conversion, this being complete for dense films and partial for macroporous counterparts. As a result, H_C increases from 148 to 1328 Oe for the macroporous films, and from 85 to 6212 Oe for the dense films. Therefore, the annealed macroporous films can be regarded as semi-hard ferromagnetic. The microstrains were of the order of 10-^{3}-10-^{4}, which are typical values for electrodeposited films [80].

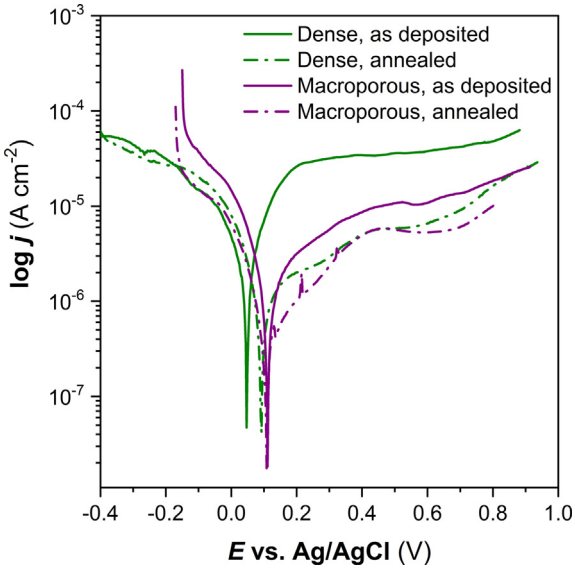

Fig. 13. PDP curves recorded in de-aerated 3.5 wt% NaCl solution for the as deposited and annealed Co-Pt films.

Table 2
E_{corr} and j_{corr} values extracted from the PDP curves of Fig. 13.

	E_{corr} (mV vs. Ag/AgCl)	j_{corr} (μA cm^{-2})
As-deposited dense film	47	16
Annealed dense film	92	3.8
As-deposited macroporous film	111	5.9
Annealed macroporous film	109	2.2

Finally, electrochemical corrosion tests were carried out to disclose, if so, differences in the corrosion behavior of the coatings. Fig. 13 shows the PDP curves of the as-deposited and annealed Co-Pt films in 3.5 wt.% NaCl solution. The samples showed similar E_{corr} values in the range between 50 mV and 111 mV. Interestingly, the macroporous samples showed slightly more positive E_{corr} values than their dense counterparts. The naked Si/Ti substrate gave a significantly more negative E_{corr} value of −131 mV, hence the PDP curves are quite representative of the behavior of the Co–Pt films. The j_{corr} values were in the range of a few μA cm^{-2} (see Table 2). Importantly, the corrosion resistance of the macroporous films did not deteriorate in spite of the remarkable increase in the surface-to-volume (S/V) ratio. Yet, the real surface area of the macroporous films is unknown and, hence, the current density values are not fully meaningful. Vallés and co-workers measured E_{corr} values between −130 mV and + 30 mV vs. Ag/AgCl in 5.0 wt.% NaCl for Co-Pt deposits depending on their crystalline structure (fcc or hcp) and Pt content (39 wt.% – 77 wt.%) [81]. Hence, our values are in agreement with the literature.

4. Conclusions

Macroporous, semi-hard-magnetic Co-Pt thin films were prepared by colloidal crystal template-assisted electrodeposition from an aqueous sulfate–chloride electrolyte followed by annealing. A parametric study of the optimal annealing conditions taking electrodeposited dense counterparts as a reference revealed that a maximum H_C value of 1328 Oe was achieved after annealing at 600 °C for 80 min. Importantly, the selected patterning method (colloidal crystal templating) and bead size (215 nm) secured the preservation of porosity in the Co-Pt films upon annealing. Other patterning approaches and/or smaller pore sizes could result in pore collapse. GIXRD analyses evidenced the polycrystalline structure of the as-deposited macroporous films, which showed a nearly equiatomic A1-disordered Co-Pt solid solution with some additional minor phases. In turn, the existence of different magnetic and crystallographic phases (hard-magnetic Pt-rich $L1_0$-ordered and soft-magnetic A1-disordered and $CoPt_3$ phases) was seen in the annealed macroporous films. Potentiodynamic polarization curves were indicative of the noble character of the films. The increase of the S/V ratio brought by the introduction of porosity in the Co-Pt films was not deleterious for the corrosion resistance. This study demonstrates that the combination of electrodeposition and colloidal templating technique is a suitable strategy for fabricating semi-hard-magnetic porous (and hence, more lightweight) films. These materials are appealing as low-density magnets or magnetic composites with a great potential for implementation in spacecraft, automobile or magnetoelectric devices. This synthetic strategy could be well extended to other $L1_0$-ordered alloys (i.e., Co-Pd, Fe-Pt and Fe-Pd). Also, because of the presence of noble metals and large S/V ratio, the macroporous films could be used for electrocatalytic purposes like the hydrogen evolution reaction.

Declaration of Competing Interest

The authors declare that they have no known competing financial interests or personal relationships that could have appeared to influence the work reported in this paper.

Acknowledgements

This work was funded by the Spanish Government (Project MAT2017-86357-C3-1-R, PID2020-116844RB-C21 and associated FEDER), the Generalitat de Catalunya (2017-SGR-292), and the European Research Council (SPIN-PORICS 2014-Consolidator Grant, Agreement n. 648454).

Data availability

The raw/processed data required to reproduce these findings cannot be shared at this time as the data also forms part of an ongoing study. The data that support the findings of this study are available from the corresponding authors on request.

Appendix A. Supplementary data

Supplementary data to this article can be found online at https://doi.org/10.1016/j.matdes.2021.110369.

References

[1] T.-S. Chin, Permanent magnet films for applications in microelectromechanical systems, J. Magn. Magn. Mater. 209 (1-3) (2000) 75–79, https://doi.org/10.1016/S0304-8853(99)00649-6.
[2] A. Philip, J.-P. Niemelä, G.C. Tewari, B. Putz, T.E.J. Edwards, M. Itoh, I. Utke, M. Karppinen, Flexible ε-Fe_2O_3-terephthalate thin-film magnets through ALD/MLD, ACS Appl. Mater. Interfaces 12 (19) (2020) 21912–21921, https://doi.org/10.1021/acsami.0c0466510.1021/acsami.0c04665.s001.
[3] R.A. Murphy, J.R. Long, T.D. Harris, A hard permanent magnet through molecular design, Commun. Chem. 4 (2021) 70, https://doi.org/10.1038/s42004-021-00509-y.
[4] E.A. Kervendal, D.R. Kirk, R.B. Meinke, Spacecraft radiation shielding using ultralightweight superconducting magnets, J. Spacecr. Rockets 46 (5) (2009) 982–988, https://doi.org/10.2514/1.37490.
[5] M. Gich, L.I. Casas, A. Roig, E. Molins, J. Sort, S. Suriñach, M.D. Baró, J.S. Muñoz, L. Morellon, M.R. Ibarra, J. Nogués, High-coercivity ultralight transparent magnets, Appl. Phys. Lett. 82 (24) (2003) 4307–4309, https://doi.org/10.1063/1.1578538.
[6] M. Janulevicius, V. Klimkevičius, L. Mikoliunaite, B. Vengalis, R. Vargalis, S. Sakirzanovas, V. Plausinaitiene, A. Zilinskas, A. Katelnikovas, Ultralight magnetic nanofibrous $GdPO_4$ aerogel, ACS Omega 5 (23) (2020) 14180–14185, https://doi.org/10.1021/acsomega.0c0198010.1021/acsomega.0c01980.s001.
[7] N. Chen, Q. Pan, Versatile fabrication of ultralight magnetic foams and application for oil–water separation, ACS Nano 7 (8) (2013) 6875–6883, https://doi.org/10.1021/nn4020533.
[8] Y. Li, Q. Liu, A.J. Hess, S. Mi, X. Liu, Z. Chen, Y. Xie, I.I. Smalyukh, Programmable ultralight magnets via orientational arrangement of ferromagnetic nanoparticles within aerogel hosts, ACS Nano 13 (12) (2019) 13875–13883, https://doi.org/10.1021/acsnano.9b04818.
[9] D.P. Arnold, N. Wang, Permanent magnets for MEMS, J. Microelectromechanical Syst. 18 (2009) 1255–1266, https://doi.org/10.1109/JMEMS.2009.2034389.
[10] J. Chen, L. Rissing, Electroplating hard magnetic SmCo for magnetic microactuator applications, J. Appl. Phys. 109 (7) (2011) 07A766, https://doi.org/10.1063/1.3565414.
[11] M. Xie, Electrodeposition of Sm-Co alloy films with nanocrystalline/amorphous structures from a sulphamate aqueous solution, Int. J. Electrochem. Sci. 12 (2017) 11330–11342, https://doi.org/10.20964/2017.12.07.
[12] L. Kang, C. Cui, W. Yang, Y. Zhang, M. Guo, The properties and microstructure of Nd-Fe-B nanowires fabricated by electrochemical deposition using porous alumina templates, Mater. Chem. Phys. 242 (2020) 122470, https://doi.org/10.1016/j.matchemphys.2019.122470.
[13] X. Xu, S. Sturm, J. Zavasnik, K.Z. Rozman, Electrodeposition of a rare-earth iron alloy from an ionic-liquid electrolyte, ChemElectroChem 6 (11) (2019) 2860–2869, https://doi.org/10.1002/celc.201900286.
[14] P. Cojocaru, L. Magagnin, E. Gomez, E. Vallés, Using deep eutectic solvents to electrodeposit CoSm films and nanowires, Mater. Lett. 65 (23-24) (2011) 3597–3600, https://doi.org/10.1016/j.matlet.2011.08.003.
[15] G. Panzeri, M. Tresoldi, C. Rinaldi, L. Magagnin, Electrodeposition of magnetic SmCo films from deep eutectic solvents and choline chloride-ethylene glycol mixtures, J. Electrochem. Soc. 164 (13) (2017) D930–D933, https://doi.org/10.1149/2.0111714jes.
[16] A. Kashyap, R. Skomski, A.K. Solanki, Y.F. Xu, D.J. Sellmyer, Magnetism of $L1_0$ compounds with the composition MT (M=Rh, Pd, Pt, Ir and T=Mn, Fe Co, Ni), J. Appl. Phys. 95 (11) (2004) 7480–7482, https://doi.org/10.1063/1.1687631.

[17] R. Skomski, Phase formation in $L1_0$ magnets, J. Appl. Phys. 101 (9) (2007) 09N517, https://doi.org/10.1063/1.2711801.

[18] F.M.F. Rhen, J.M.D. Coey, Electrodeposition of coercive $L1_0$ FePt magnets, J. Magn. Magn. Mater. 322 (9-12) (2010) 1572–1575, https://doi.org/10.1016/j.jmmm.2009.09.027.

[19] Y.H. Huang, H. Okumura, G.C. Hadjipanayis, D. Weller, CoPt and FePt nanowires by electrodeposition, J. Appl. Phys. 91 (10) (2002) 6869, https://doi.org/10.1063/1.1447524.

[20] European Commission (2020) 3. accessed 10 December 2021 https://op.europa.eu/en/publication-detail/-/publication/c0d5292a-ee54-11ea-991b-01aa75ed71a1/language-en.

[21] N.M. Dempsey, Hard magnetic materials for MEMS applications, in: J.P. Liu, E. Fullerton, O. Gutfleisch, D.J. Sellmyer (Eds.), Nanoscale Magnetic Materials and Applications, Springer, US, 2009, pp. 661–683. DOI:10.1007/978-0-387-85600-1_22

[22] M.R. Visokay, R. Sinclair, Direct formation of ordered CoPt and FePt compound thin films by sputtering, Appl. Phys. Lett. 66 (1995) 1692–1694. DOI: 10.1063/1.113895

[23] R.A. Ristau, K. Barmak, L.H. Lewis, K.R. Coffey, J.K. Howard, On the relationship of high coercivity and $L1_0$ ordered phase in CoPt and FePt thin films, J. Appl. Phys. 86 (1999) 4527–4533. DOI: 10.1063/1.371397

[24] O.D. Oniku, B. Qi, D.P. Arnold, Electroplated thick-film cobalt platinum permanent magnets, J. Magn. Magn. Mater. 416 (2016) 417–428, https://doi.org/10.1016/j.jmmm.2016.05.044.

[25] A. Garraud, O.D. Oniku, D.P. Arnold, Influence of temperature on the magnetic properties of electroplated L1°CoPt thick films, J. Appl. Phys. 117 (2015) 17C718, https://doi.org/10.1063/1.4913890.

[26] J. Ewing, Y. Wang, D.P. Arnold, High-current-density electrodeposition using pulsed and constant currents to produce thick CoPt magnetic films on silicon substrates, AIP Adv. 8 (5) (2018) 056711, https://doi.org/10.1063/1.5007272.

[27] S.-J. Wang, C.-H. Chen, S.-C. Chang, K.-M. Uang, C.-P. Juan, H.-C. Cheng, Growth and characterization of tungsten carbide nanowires by thermal annealing of sputter-deposited WC_x films, Appl. Phys. Lett. 85 (12) (2004) 2358–2360, https://doi.org/10.1063/1.1791322.

[28] G. Shukla, S. Angappane, Dimensional constraints favour high temperature anatase phase stability in TiO_2 nanorods, Appl. Surf. Sci. 577 (2022) 151874, https://doi.org/10.1016/j.apsusc.2021.151874.

[29] H.H. Lou, Y. Huang, Electroplating, in: S. Lee (Ed.), Encyclopedia of Chemical Processing, Taylor & Francis, New York, 2006, pp. 839–848.

[30] O.D. Oniku, B. Qi, D.P. Arnold, Electroplated L1°CoPt thick-film permanent magnets, J. Appl. Phys. 115 (2014) 17E521, https://doi.org/10.1063/1.4867119.

[31] F.M.F. Rhen, E. Backen, J.M.D. Coey, Thick-film permanent magnets by membrane electrodeposition, J. Appl. Phys. 97 (11) (2005) 113908, https://doi.org/10.1063/1.1923587.

[32] O. Berkh, Y.u. Rosenberg, Y. Shacham-Diamand, E. Gileadi, Electrodeposited near-equiatomic CoPt thick films, Electrochem. Solid-State Lett. 11 (4) (2008) D38, https://doi.org/10.1149/1.2838047.

[33] Y. Wang, J. Ewing, D.P. Arnold, Ultra-thick electroplated CoPt magnets for MEMS, J. Micro. Syst. 28 (2) (2019) 311–320, https://doi.org/10.1109/JMEMS.2018.2888846.

[34] T. Yanai, R. Hamamura, J. Honda, A. Tomita, H. Yamada, N. Fujita, K. Takashima, M. Nakano, H. Fukunaga, Electroplated Co–Pt thick-film magnets prepared in citric-acid-based plating baths, IEEE Trans. Magn. 53 (11) (2017) 1–3, https://doi.org/10.1109/TMAG.2017.2710351.

[35] K. Hosoiri, F. Wang, S. Doi, T. Watanabe, Preparation and characterization of electrodeposited Co-Pt binary alloy film, Mater. Trans. 44 (4) (2003) 653–656, https://doi.org/10.2320/matertrans.44.653.

[36] V. Georgescu, M. Daub, Magnetism and magnetoresistance in electrodeposited ($L1_0$) CoPt superlattices, J. Optoelectron. Adv. Mater. 7 (2005) 853–858.

[37] Y. Wang, R. Bowrothu, Y.-K. Yoon, D.P. Arnold, Patterning of thick electroplated CoPt magnets using SU-8 micromoulds, Micro & Nano Lett. 14 (2019) 1393–1396, https://doi.org/10.1049/mnl.2019.0287.

[38] F. Wang, K. Hosoiri, S. Doi, N. Okamoto, T. Kuzushima, T. Totsuka, T. Watanabe, Nanostructured L1°Co–Pt thin films by an electrodeposition process, Electrochem. Commun. 6 (2004) 1149–1152, https://doi.org/10.1016/j.elecom.2004.09.009.

[39] N. Yasui, A. Imada, T. Den, Electrodeposition of (001) oriented CoPt $L1_0$ columns into anodic alumina films, Appl. Phys. Lett. 83 (2003) 3347–3349, https://doi.org/10.1063/1.1622787.

[40] A. Hannour, L. Bardotti, B. Prével, F. Tournus, D. Mailly, J.-P. Bucher, A. Nafidi, Nanostructured $L1_0$-CoPt dot arrays with perpendicular magnetic anisotropy, Mater. Lett. 193 (2017) 108–111, https://doi.org/10.1016/j.matlet.2017.01.114.

[41] D.-Y. Park, N.V. Myung, Magnetic properties of electrodeposited cobalt-platinum (CoPt) and cobalt-platinum-phosphide (CoPtP) thin films, Front. Chem. 9 (2021), https://doi.org/10.3389/fchem.2021.733383 733383.

[42] Y. Li, W.-Z. Jia, Y.-Y. Song, X.-H. Xia, Superhydrophobicity of 3D porous copper films prepared using the hydrogen bubble dynamic template, Chem. Mater. 19 (23) (2007) 5758–5764, https://doi.org/10.1021/cm071738j.

[43] J. Zhang, M.D. Baró, E. Pellicer, J. Sort, Electrodeposition of magnetic, superhydrophobic, non-stick, two-phase Cu–Ni foam films and their enhanced performance for hydrogen evolution reaction in alkaline water media, Nanoscale 6 (21) (2014) 12490–12499, https://doi.org/10.1039/C4NR03200D.

[44] L. Wang, Y. Yamauchi, Strategic synthesis of trimetallic Au@Pd@Pt core–shell nanoparticles from poly(vinylpyrrolidone)-based aqueous solution toward highly active electrocatalysts, Chem. Mater. 23 (9) (2011) 2457–2465, https://doi.org/10.1021/cm200382s.

[45] B.O. Jiang, C. Li, V. Malgras, M. Imura, S. Tominaka, Y. Yamauchi, Mesoporous Pt nanospheres with designed pore surface as highly active electrocatalyst, Chem. Sci. 7 (2) (2016) 1575–1581, https://doi.org/10.1039/C5SC03779D.

[46] H. Wang, H.Y. Jeong, M. Imura, L. Wang, L. Radhakrishnan, N. Fujita, T. Castle, O. Terasaki, Y. Yamauchi, Shape- and size-controlled synthesis in hard templates: sophisticated chemical reduction for mesoporous monocrystalline platinum nanoparticles, J. Am. Chem. Soc. 133 (37) (2011) 14526–14529, https://doi.org/10.1021/ja2058617.

[47] M. Pérez-Page, E. Yu, J. Li, M. Rahman, D.M. Dryden, R. Vidu, P. Stroeve, Template-based syntheses for shape controlled nanostructures, Adv. Colloid Interface Sci. 234 (2016) 51–79, https://doi.org/10.1016/j.cis.2016.04.001.

[48] S. Rasouli, N. Rezaei, H. Hamedi, S. Zendehboudi, X. Duan, Superhydrophobic and superoleophilic membranes for oil-water separation application: A comprehensive review, Mater. Des. 204 (2021) 109599, https://doi.org/10.1016/j.matdes.2021.109599.

[49] Z.-Z. Gu, A. Fujishima, O. Sato, Fabrication of high-quality opal films with controllable thickness, Chem. Mater. 14 (2) (2002) 760–765, https://doi.org/10.1021/cm0108435.

[50] P. Jiang, T. Prasad, M.J. McFarland, V.L. Colvin, Two-dimensional nonclose-packed colloidal crystals formed by spincoating, Appl. Phys. Lett. 89 (1) (2006) 011908, https://doi.org/10.1063/1.2218832.

[51] A.L. Rogach, N.A. Kotov, D.S. Koktysh, J.W. Ostrander, G.A. Ragoisha, Electrophoretic deposition of latex-based 3D colloidal photonic crystals: a technique for rapid production of high-quality opals, Chem. Mater. 12 (2000) 2721–2726, https://doi.org/10.1021/cm000274l.

[52] P.V. Braun, P. Wiltzius, Electrochemically grown photonic crystals, Nature 402 (6762) (1999) 603–604, https://doi.org/10.1038/45137.

[53] D.W. Bruce, D. O'Hare, R.I. Walton, Porous Materials, John Wiley & Sons, UK, Inorganic Materials Series, 2010.

[54] A. Nicolenco, Y.u. Chen, N. Tsyntsaru, H. Cesiulis, E. Pellicer, J. Sort, Mechanical, magnetic and magnetostrictive properties of porous Fe-Ga films prepared by electrodeposition, Mater. & Design 208 (2021) 109915, https://doi.org/10.1016/j.matdes.2021.109915.

[55] A. Baux, G. Couégnat, G.L. Vignoles, D. Lasseux, A. Kuhn, C. Carucci, N. Mano, T. D. Le, Digitization and image-based structure-properties relationship evaluation of a porous gold micro-electrode, Mater. & Des. 193 (2020) 108812, https://doi.org/10.1016/j.matdes.2020.108812.

[56] R. Ramachandramoorthy, M. Mieszala, C.V. Manzano, X. Maeder, J. Michler, L. Philippe, Dual-templated electrodeposition and characterization of regular metallic foam based microarchitectures, Appl. Mater. Today 20 (2020) 100667, https://doi.org/10.1016/j.apmt.2020.100667.

[57] F. Li, D. Wang, Q. Liu, B. Wang, W. Zhong, M. Li, K. Liu, Z. Lu, H. Jiang, Q. Zhao, C. Xiong, The construction of rod-like polypyrrole network on hard magnetic porous textile anodes for microbial fuel cells with ultra-high output power density, J. Power Sources 412 (2019) 514–519, https://doi.org/10.1016/j.jpowsour.2018.11.090.

[58] S.M. Jones, Aerogel: Space exploration applications, J. Sol-Gel Sci. Technol. 40 (2-3) (2006) 351–357, https://doi.org/10.1007/s10971-006-7762-7.

[59] J. Sort, J. Nogués, X. Amils, S. Suriñach, J.S. Muñoz, M.D. Baró, Room temperature coercivity enhancement in mechanically alloyed antiferromagnetic-ferromagnetic powders, Appl. Phys. Lett. 75 (20) (1999) 3177–3179, https://doi.org/10.1063/1.125269.

[60] J. Nogués, I.K. Schuller, Exchange bias, J. Magn. Magn. Mater. 192 (2) (1999) 203–232, https://doi.org/10.1016/S0304-8853(98)00266-2.

[61] L. Luterotti, P. Scardi, Simultaneous structure and size-strain refinement by the Rietveld method, J. Appl. Crystallogr. 23 (1990) 246–252, https://doi.org/10.1107/S0021889890002382.

[62] N.V. Myung, D.-Y. Park, B.-Y. Yoo, P.T.A. Sumodjo, Development of electroplated magnetic materials for MEMS, J. Magn. Magn. Mater. 265 (2) (2003) 189–198, https://doi.org/10.1016/S0304-8853(03)00264-6.

[63] K. Eiler, S. Suriñach, J. Sort, E. Pellicer, Mesoporous Ni-rich Ni–Pt thin films: Electrodeposition, characterization and performance toward hydrogen evolution reaction in acidic media, Appl. Catal. B Environ. 265 (2020) 118597, https://doi.org/10.1016/j.apcatb.2020.118597.

[64] K. Leistner, S. Oswald, J. Thomas, S. Fähler, H. Schlörb, L. Schultz, Potential dependence of composition and structure of electrodeposited Fe–Pt films, Electrochim. Acta 52 (1) (2006) 194–199, https://doi.org/10.1016/j.electacta.2006.04.058.

[65] A. Nicolenco, N. Tsyntsaru, H. Cesiulis, Fe (III)-based ammonia-free bath for electrodeposition of Fe-W alloys, J. Electrochem. Soc. 164 (9) (2017) D590–D596, https://doi.org/10.1149/2.1001709jes.

[66] I. Golvano-Escobal, R. de Paz-Castany, C.C.J. Alcantara, S. Pané, E. Garcia-Lecina, J. Sort, E. Pellicer, Functional macroporous iron-phosphorous films by electrodeposition on colloidal crystal templates, Electrochim. Acta 313 (2019) 211–222, https://doi.org/10.1016/j.electacta.2019.05.009.

[67] T. Müller, J. Grimwood, A. Bachmaier, R. Pippan, Electrodeposition of Fe-C alloys from citrate baths: structure, mechanical properties, and thermal stability, Metals 8 (2018) 363, https://doi.org/10.3390/met8050363.

[68] I.N. Krivorotov, H. Yan, E.D. Dahlberg, A. Stein, Exchange bias in macroporous Co/CoO, J. Magn. Magn. Mater. 226–230 (2001) 1800–1802, https://doi.org/10.1016/S0304-8853(00)00934-3.

[69] K.Ž. Rožman, J. Kovač, P.J. McGuiness, Z. Samardžija, B. Markoli, S. Kobe, Microstructural, compositional and magnetic characterization of

electrodeposited and annealed Co–Pt-based thin films, Thin Solid Films 518 (6) (2010) 1751–1755, https://doi.org/10.1016/j.tsf.2009.11.025.
[70] X. Sun, Z.Y. Jia, Y.H. Huang, J.W. Harrell, D.E. Nikles, K. Sun, L.M. Wang, Synthesis and magnetic properties of CoPt nanoparticles, J. Appl. Phys. 95 (11) (2004) 6747–6749, https://doi.org/10.1063/1.1667441.
[71] S. Jeong, Y.-N. Hsu, D.E. Laughlin, M.E. McHenry, Atomic ordering and coercivity mechanism in FePt and CoPt polycrystalline thin films, IEEE Trans. Magn. 37 (2001) 1299, https://doi.org/10.1109/20.950823.
[72] T. Yanai, J. Honda, R. Hamamura, Y. Omagari, H. Yamada, N. Fujita, K. Takashima, M. Nakano, H. Fukunaga, Improvement in surface conditions of electroplated Fe-Pt thick-film magnets, AIP Adv. 8 (5) (2018) 056437, https://doi.org/10.1063/1.5007196.
[73] K. Leistner, J. Thomas, H. Schlörb, M. Weisheit, L. Schultz, S. Fähler, Highly coercive electrodeposited FePt films by postannealing in hydrogen, Appl. Phys. Lett. 85 (16) (2004) 3498–3500, https://doi.org/10.1063/1.1807958.
[74] Y. Ying, H. Wang, J. Zheng, J. Yu, W. Li, L. Qiao, W. Cai, S. Che, Preparation, microstructure, and magnetic properties of electrodeposited nanocrystalline $L1_0$ FePt films, J. of Supercon. Nov. Magn. 33 (11) (2020) 3563–3570, https://doi.org/10.1007/s10948-020-05624-w.
[75] K. Žužek Rožman, A. Krause, K. Leistner, S. Fähler, L. Schultz, H. Schlörb, Electrodeposition and hard magnetic properties of Co–Pt films in comparison to Fe–Pt films, J. Magn. Magn. Mater. 314 (2) (2007) 116–121, https://doi.org/10.1016/j.jmmm.2007.02.146.
[76] C. Navarro-Senent, J. Fornell, E. Isarain-Chávez, A. Quintana, E. Menéndez, M. Foerster, L. Aballe, E. Weschke, J. Nogués, E. Pellicer, J. Sort, Large magnetoelectric effects in electrodeposited nanoporous microdisks driven by effective surface charging and magneto-ionics, ACS Appl. Mater. Interfaces 10 (51) (2018) 44897–44905, https://doi.org/10.1021/acsami.8b1744210.1021/acsami.8b17442.s001.
[77] DongEung Kim, J.E. Saal, L. Zhou, ShunLi Shang, Y. Du, Z.-K. Liu, Thermodynamic modeling of fcc order/disorder transformations in the CoPt system, CALPHAD 35 (3) (2011) 323–330, https://doi.org/10.1016/j.calphad.2011.04.005.
[78] X.B. Liu, Z. Altounian, Exchange interaction in $L1_0$-ordered FePt and CoPt from first-principles, J. Appl. Phys. 109 (7) (2011) 07B762, https://doi.org/10.1063/1.3564953.
[79] J.F. Moulder, W.F. Stickle, P.E. Sobol, K.D. Bomben, Handbook of X-ray photoelectron spectroscopy, Physical Electronics Inc, MI, 1995.
[80] E. Pellicer, A. Varea, S. Pané, K.M. Sivaraman, B.J. Nelson, S. Suriñach, M.D. Baró, J. Sort, Sort, A comparison between fine-grained and nanocrystalline electrodeposited Cu–Ni films. Insights on mechanical and corrosion performance, Surf. Coat Technol. 205 (23-24) (2011) 5285–5293, https://doi.org/10.1016/j.surfcoat.2011.05.047.
[81] M. Cortés, E. Gómez, E. Vallés, Magnetic properties of nanocrystalline CoPt electrodeposited films. Influence of P incorporation, J. Sol. State, Electrochem. 14 (12) (2010) 2225–2233, https://doi.org/10.1007/s10008-010-1055-3.